Non-redundant Raman imaging using optical eigenmodes

Sebastian Kosmeier, Svetlana Zolotovskaya, Kishan Dholakia, and Michael Mazilu

SUPA, School of Physics and Astronomy, University of St Andrews, North Haugh, KY16 9SS, St Andrews, UK

Anna Chiara De Luca

Institute of Protein Biochemistry, National Research Council,
Via P. Castellino 111, 80313, Naples , Italy and
To whom correspondence should be addressed; a.deluca@ibp.cnr.it

Andrew Riches

School of Medicine, University of St Andrews, North Haugh, KY16 9TF, St Andrews, UK

C. Simon Herrington

Medical Research Institute, University of Dundee,
Ninewells Hospital Medical School, James Arrott Drive, DD1 9SY, Dundee, UK
(Dated: 17 October 2014)

Various forms of imaging schemes have emerged over the last decade that are based on correlating variations in incident illuminating light fields to the outputs of single 'bucket' detectors. However, to date, the role of the orthogonality of the illumination fields has largely been overlooked and furthermore, the field has not progressed beyond bright field imaging. By exploiting the concept of orthogonal illuminating fields, we demonstrate the application of optical eigenmodes (OEi) to wide field, scan-free spontaneous Raman imaging, which is notoriously slow in wide-field mode. The OEi approach enables a form of indirect imaging that exploits both phase and amplitude in image reconstruction. The use of orthogonality enables us to non-redundantly illuminate the sample and, in particular, use a subset of illuminating modes to obtain the majority of information from the sample, thus minimising any photobleaching or damage of the sample. The crucial incorporation of phase, in addition to amplitude, in the imaging process significantly reduces background noise and results in an improved SNR for the image while reducing the number of illuminations. As an example we can reconstruct images of a surface-enhanced Raman spectroscopy (SERS) active sample with approximately an order of magnitude fewer acquisitions. This generic approach may readily be applied to other imaging modalities such as fluorescence microscopy or nonlinear vibrational microscopy.

I. INTRODUCTION

A generic challenge in all forms of imaging is to acquire information in a rapid, damage-free manner. In the optical domain, photo-damage can be an issue in numerous forms of biomedical methods and furthermore the very manner of sample illumination is typically non-optimal. In this context, structured illumination aims to engineer the excitation/illumination beams to achieve either faster acquisition [1], higher resolution [2, 3] or even 3D imaging capabilities [4]. Structured illumination in combination with 'bucket' detection (single detector acquisition) has gained popularity due to its inherent simplicity. Separately, illumination based upon non-redundant imaging relies on the use of structured light fields incident on a sample to detect its features by using the smallest number of illuminations i.e. to achieve the fastest acquisition. This is normally not the case when considering a scanned Gaussian beam approach where the partial overlap between adjacent excitation spots leads to no additional information ('redundant' measure) and to a decreased image resolution. Due to their orthogonality, optical eigenmodes (OEi) offer a natural set of fields that avoid any overlap in the probing the optical degrees of freedom of the sample [5, 6]. Additionally, the experimental *in situ* determination of the optical eigenmodes has the advantage of automatically taking into account all optical aberrations present in the optical system. It is therefore advantageous to use these OEi as structured illumination fields in the context of imaging.

Previously, we have developed a coherent indirect imaging technique [7] based on OEi fields. This paper demonstrates the first experimental application of this approach to the case of imaging spontaneous Raman scattering. In particular, Raman scattering is a vibrational microscopy method offering a label-free imaging contrast mechanism capable of probing non-invasively the chemical composition of biological and inert materials at microscopic scales [8–12]. It has promise for many applications yet has been hampered by long acquisition times which in turn has resulted in researchers resorting typically to more complex nonlinear vibrational spectroscopy methods.

Standard laser scanning based Raman spectroscopic imaging [13, 14] allows the quantification of the chemical heterogeneity of a sample in terms of the spatial distribution of its molecular constituents. For these reasons, Raman imaging applications cover a wide range of scientific disciplines such as, pharmacology, biology, medicine

and material science [15–18]. Importantly, Raman imaging is useful to measure the pharmacokinetic properties of tablets as well as aid in authenticity evaluation, manufacturing processes, biomedical imaging and even in counterfeit product identification [19]. However, there exists a trade-off between the achievable scanning based imaging speed and the spectral selectivity of such schemes. Raman spectroscopy is notoriously slow and not usually suitable for wide field imaging purposes as the signals are very weak (only one photon in one million is Raman scattered). The required detection times are of the order of seconds to minutes for each pixel. As a result, an image of an area of tens of micrometers in length and width typically requires hours to acquire, making micro-Raman not suitable for rapid large-scale imaging of pharmaceutical tablets as an example. Various Raman imaging methodologies have been proposed to alleviate this issue. In point and line scanning Raman imaging [13, 14, 20, 21] a circular or line shaped laser spot raster scans the sample in two spatial dimensions with a Raman spectrum recorded at each position.

Other direct imaging techniques illuminate the sample using a number of laser spots or a wide-field laser beam. The resulting Raman signal is directly imaged on a filtered detector acquiring a single measurement. For example in [22], the authors used an Hadamard mask to produce structure illumination pattern on the sample to generate only one-dimensional compressed Raman image. Additional wide-field Raman approaches include tuneable detection band-pass filters and two-dimensional detector [23–25]. However, this method discards the Raman scattered photons outside the wavelength detection band rendering this approach spectrally inefficient. Recently, a multivariate hyperspectral Raman imaging (MHRI) approach has been introduced by Davis et al. based on a compressive spectral detection strategy [26]. Our approach applies a non-redundant approach to the illumination side of the Raman imaging enabling a step change in the acquisition process for this modality. This non-redundant approach is equivalent to a compression in the number of measures when comparing to a standard raster scan method. This is due to the fact that the standard raster scan approach inherently leads to an overlap between adjacent optical beams.

In our non-redundant Raman OEi imaging, we illuminate the sample with a predetermined set of optical eigenmodes. For each of the illuminations used, we measure the Raman spectrum from which we subsequently reconstruct the hyperspectral Raman image of the sample. An important outcome of this method is the adaptive resolution that can be achieved. Indeed, to increase the resolution, we do not need to rescan the sample with a finer step size but simply continue to probe the sample with increasingly higher order OEi illuminations. In effect, the higher the order of the OEi illumination, the finer the details probed by the OEi illumination. Furthermore, due to the non-redundant nature of OEi based structured illumination, we realise a given imaging resolution using the smallest number of OEi probes possible. Similar arguments are also employed when considering compressive fluorescence imaging [27]. The sparsity of the sample allows it to be imaged using a small number of illuminations. Here, we restrict the number of illuminations such that the sparse degrees of freedom of the optical setup are used optimally for probing from the onset delivering a non-redundant version of compressive imaging. Interestingly, our approach is also similar to "computational ghost imaging" whereby known fields are used to illuminate a sample and the image is reconstructed using the scattering coefficients [28, 29]. However, here the light is not shaped by a random mask created by a diffuser or spatial light modulator (SLM) but the illuminations correspond to a non-redundant set of orthogonal optical eigenmode beam profiles.

II. RESULTS

a. Determining the OEi. Figure 1a describes our experimental set-up. Figure 1b shows the theoretical spatial field distribution of the first nine Optical Eigenmodes $\mathbb{E}_\ell$ in the region of interest (ROI) [7, 30]. We observe that as the order of the mode ℓ increases finer details are accessed. In order to check the orthonormality relation, in the region of interest (ROI), $\int_{\text{ROI}} \mathbb{E}_k \mathbb{E}_l^* d\sigma = \delta_{kl}$ of the experimentally implemented OEi, the complex product $\mathbb{E}_k \mathbb{E}_l^*$ is determined from four intensity acquisitions according to the polarization identity [31]. Each entry in the matrix in Fig. 1c corresponds to an orthonormality relation for a pair k, l. The matrix is almost diagonal, hence demonstrating orthonormality of the experimentally implemented modes in good approximation (for more details see the Methods section). Remark that the presence of high aberrations precludes the use of theoretically calculated eigenmodes, however, in this case these eigenmodes can be experimentally determined [5] automatically accounting for any aberration and angular dependance.

b. Raman OEi imaging. As a first example, we imaged a sample consisting of a polystyrene bead in the top right corner of the ROI and a PMAA bead in the lower left corner, both beads are 3 μm in diameter. Figure 2b shows a brightfield image of the sample. Figures 2c and 2d depict raster scan Raman images of the sample obtained by integrating the main polystyrene and PMAA peaks, respectively (shown in Fig. 2a). In Fig. 2e the information from Fig. 2c and Fig. 2d are superimposed in a hyperspectral image, highlighting the polystyrene bead (red color) and the PMAA bead (in blue).

Following the raster scans, the same object was imaged with the OEi approach, using only the first $M = 4$ modes, where M was chosen such as to deliver a signal to noise ratio (SNR) comparable to the raster-scan image (SNR defined later). The results are shown in Figs. 2f and 2g with the reconstruction carried out for the polystyrene and PMAA peaks, respectively. Fig. 2h depicts the hy-
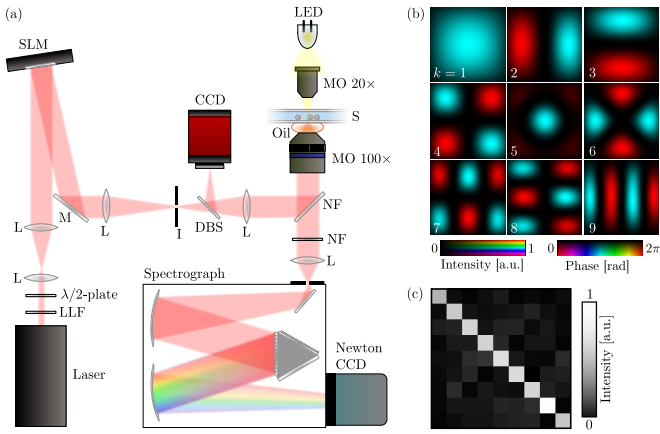
FIG. 1. (a) Experimental configuration for Optical Eigenmode Raman microscopy. LLF: Laser line filter at 785 nm; L: Lens; SLM: Spatial light modulator; M: Mirror; I: Iris to filter out first diffraction order from SLM; DBS: Dichroic beam splitter reflecting visible light and transmitting infrared light; CCD: CCD camera; NF: Notch filters to transmit Raman scattered light into the spectrograph; MO: Microscope objective; S: Sample. (b) Spatial field distribution and (c) orthogonality matrix of the first nine OEi.
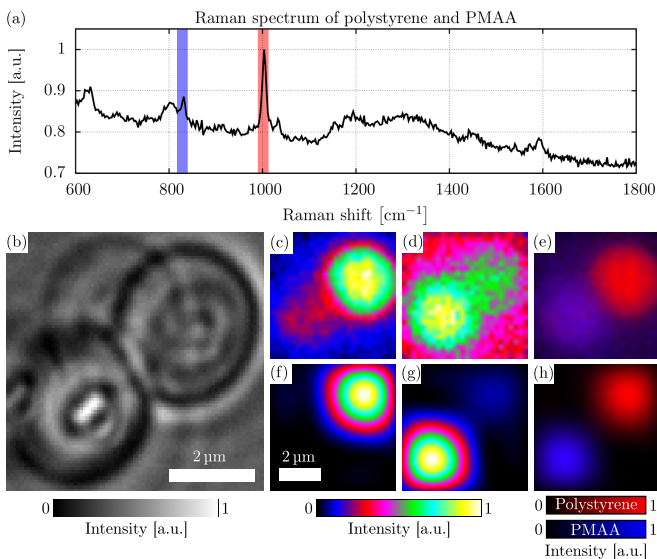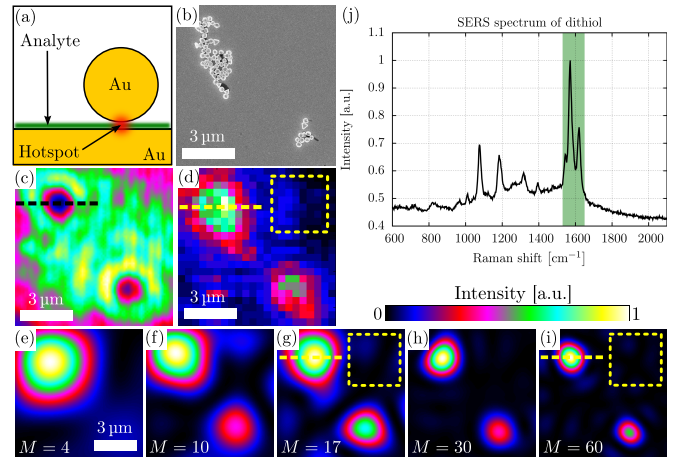

FIG. 3. (a) Schematic of the SERS sample: 200 nm gold particle on a gold surface coated with the analyte dithiol. The hotspot between the gold layer and the sphere gives rise to a SERS signal. (b) SEM image of a sample area similar to the imaged one. (c) Reflected laser light from the 9 μm × 9 μm ROI chosen for imaging. Two agglomerates of gold particles are visible as dark spots. (d) SERS Raman raster scan of the sample plane. (e-i) OEi imaging reconstruction for $M = 4$ to $M = 60$ modes. (j) SERS spectrum of dithiol.

FIG. 2. (a) Spectrum for one polystyrene bead and one PMAA bead illuminated with the 4th eigenmode and 3 s acquisition time. The area of the PMAA peak is indicated in blue while that of polystyrene is highlighted in red. (b) White-light image of the sample with a polystyrene bead in the top right corner and a PMAA bead in the lower left corner. (c), (d) Raman images obtained with 26×26 points raster scans. (f), (g) OEi Raman images corresponding to (c) and (d). (e) Graphical superposition of the intensity distributions in (c) and (d), showing the positions of the polystyrene bead (red) and the PMAA bead (blue). (h) The same as (e) for the OEi images.
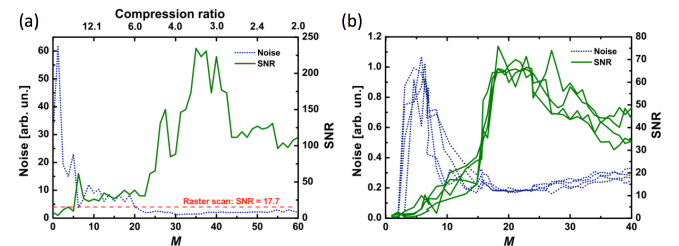

FIG. 4. (a) Experimental signal to noise ratio (SNR) and noise level as a function on the number of OEi illuminations. (b) Theoretical SNR and noise level as a function on the number of OEi illuminations for a system paraxial optical stochastically system including CCD readout, SLM beam creation and optical system noise.

perspectral Raman OEi image. Both beads are clearly reconstructed in agreement with the standard raster scans, hence demonstrating the functionality of the method and its non-redundant nature. Furthermore, we remark that the OEi images visually exhibit a lower background noise compared to the raster scans.

c. SERS OEi imaging. In order to investigate the capabilities of the method to image samples with more highly resolved features, agglomerates of 200 nm gold nanoparticles were chosen as sample objects. The nanoparticles were deposited on a gold surface covered with an analyte, in our case dithiol [32, 33]. The small gap of less than 2 nm between the gold surface and the gold particles enables a strong field enhancement, giving rise to surface enhanced Raman scattering (SERS).

Fig. 3a shows a sketch of this arrangement with a gold sphere on the gold surface. As the object for the following experiments we chose a sample region with two agglomerates of particles. The scanning electron microscope (SEM) image in Fig. 3b shows an area of the sample, which is similar to the one we used for imaging. The actual object configuration is displayed in Fig. 3c, which is a reflection of the reference wave E_{ref} from the sample surface. The nanoparticle agglomerates appear with low intensity due to scattering. The main Raman peak of dithiol is located at a Raman shift of about $1600\,cm^{-1}$ (Fig. 3j, area of integration highlighted in green). SERS raster scan using 22×22 pixels results in the image shown in Fig. 3d, revealing the SERS activity at the position of the gold particle agglomerates. The corresponding OEi based images are depicted in Figs. 3e to 3i for projection of $M = 4$ to $M = 60$ modes.

d. Signal to noise ratio. In Fig. 3, we observe visually that increasing the number M of OEi used, the location and size of the SERS hotspots is reproduced with more accuracy. This effect can be quantified experimentally Fig. 4a and theoretically Fig. 4b by measuring the changes in the SNR and noise level as a function of the number of OEi illuminations used. The SNR is defined as the ratio between maximum Raman peak, in the high signal region, and the average signal from the image region void of Raman active medium where any measured signal can be associated with system noise. To determine the experimental SNR, we used the maximum Raman peak of the image divided by the mean value in the dotted squares in Figs. 3d,i for the raster scan and for the OEi image respectively. Note that, by adjusting the exposure time for each acquisition accordingly, the total laser power used to obtain both methods was identical. The results from the numerical simulation presented in Fig. 4b illustrate the case of a paraxial optical system consisting of a phase and amplitude mask for the SLM, an apertured lens modelling a generic finite optical system and the imaging plane corresponding to the Fourier plane with respect to the SLM plane. The model takes into account noise in the system (beam pointing stability and detection) for both the determination and the subsequent use of the OEi for imaging. Multiple numerical realisations are shown to visualise the effect of the noise.

e. Pharmaceutical applications. Finally, the applicability of the Raman OEi imaging was investigated in a pharmaceutical context. In particular, the compound distribution of the well-known anticongestion and analgesic compound SUDAFED (Wrafton Laboratories Ltd) was determined. Each capsule contains a microcrystal mixture of paracetamol (500 mg), caffeine (25 mg), and phenylephrine hydrochloride (6.1 mg). A white-light full field image of the sample is shown in Fig. 5a. The ROI of $3.6 \times 3.6\,\mu m$, marked with the white square, includes two adjacent microcrystals. Fig. 5b shows a typical Raman spectrum of the two compounds illuminated simultaneously by $\ell = 12$ OEi. The reconstructions, based on the coupling coefficients of the Raman bands unique for each
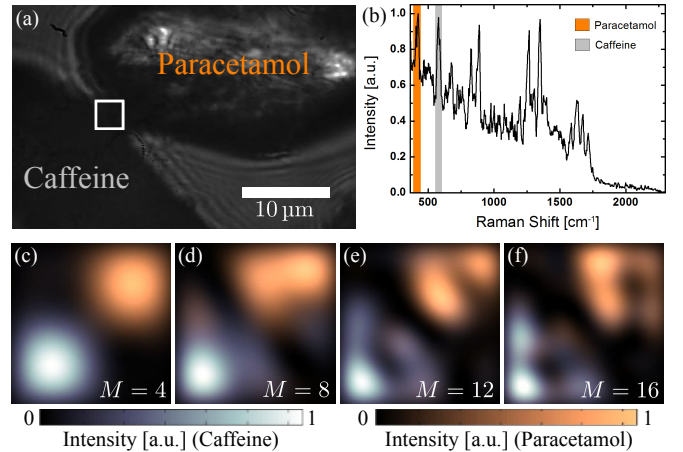

FIG. 5. (a) Full field of view image of a SUDAFED sample: A paracetamol crystal (top right corner) and a caffeine crystal (bottom left corner). The white square indicates the ROI. (b) Spectrum of the compound sample, in the ROI, illuminated with the 12th OEi mode, 5 s acquisition time and $250\,\mu m$ slit width. (c-f) Hyperspectral images of the ROI for different number M of OEis.

compound, are depicted in Figs. 5c to 5f for $M = 4$ to $M = 16$ modes. It can be seen that two substances are clearly resolved.

III. DISCUSSION

The decomposition of the focal field into eigenmodes enables illumination of the object in its most nonredundant possible manner. The number of OEi illuminations (M) necessary is determined by the criteria chosen such as resolution or SNR. This number can either be done initially for an unknown sample by considering the optical coupling efficiency to each of the OEi or adaptively during the imaging process. Experimentally, hyperspectral Raman indirect imaging was shown for an object containing beads of different materials (Fig. 2) and hence different Raman signatures. In this case, we achieved a Raman image using only $M = 4$ OEi. In real terms, this corresponds to 16 illumination fields compared to $26 \times 26 = 676$ illuminations for the raster scan methods (Fig. 2d) delivering a compression of more then 40 times. Additionally, the OEi imaging concept was applied to a SERS sample (Fig. 3) and compared to raster scanning imaging as the native Raman imaging modality. In this case, by comparing the raster scan image with the $M = 17$ image in Fig. 3g, which shows a similar reconstruction, we observe a 7-fold compression ratio. This compression ratio still delivers a large improvement versus the traditional raster scan method albeit this is not as high as in the case of beads due to the present reproducibility issues with SERS substrates. The compression ratio can further be improved by a factor of 4 when detecting the complex field in the image

plane using a holographic approach [34] as opposed to the polarization identity [31].

A further advantage of the method presented here is the improvement in the signal to noise ratio (SNR). If we look at the SERS experimental data (Fig. 3), for $M = 60$ modes good visual agreement of the OEi image (Fig. 3i) and the reference image (Fig. 3c) is observed. As for the images of the beads, the OEi images of the SERS sample exhibit a lower background than the raster scans. This visual impression was confirmed quantitatively in terms of the SNR (see Fig. 4a). With a value of 17.7, the SNR in the raster scan is an order of magnitude lower compared to the value of 245 measured in the OEi image. Fig. 4a also shows that increasing the number of OEi illuminations implies an increase of the SNR. A maximum (in this case at $M = 35$) is achieved when the noise level drops below a certain measurement resolution threshold (determined by considering the readout noise of the detector and its dynamic range). Additionally, each OEi mode is associated with a optical coupling efficiency (eigenvalue) linking the SLM beam generation plane to the imaging plane. As the OEi modes are ordered by decreasing eigenvalues, the larger the mode number the more difficult it becomes to create efficiently the corresponding OEi beam. This can also be seen in the slight increase in the noise level in Fig. 4.

An important aspect of any imaging method is its resolution. We investigated this factor by measuring the full width at half maximum of the larger of the two SERS clusters (dashed lines in Figs. 3c, 3d, 3g and 3i). The optical image used as reference image shows a width of $w_{\text{ref}} = 1.58 \, \mu\text{m}$. The raster scan image measures this particle agglomerate with a width of $w_{\text{ras}} = 2.57 \, \mu\text{m}$. This deviation is attributed to the background noise and the 400 nm step width of the raster scan, which was chosen for a good compromise between SNR and spatial resolution. In contrast, the Raman OEi imaging scheme does not rely on probing the sample at discrete points, but uses a continuous wide-field sample illumination. As a result, the width $w_{\text{OEi},M=60} = 1.30 \, \mu\text{m}$ measured for the OEi image is in good agreement with the reference width w_{ref}. Further, adaptive resolution can be implemented using OEi illuminations. As shown in Figures 3 and 5, it is possible to continuously increase the image resolution by illuminating the sample with increasing higher order OEi without rescanning the sample.

It is by combining the SNR and resolution arguments that we can quantify the compression/non-redundancy level achieved by the OEi method discussed previously. Indeed, for determining the compression factor in the SERS case (Fig. 3), we look for the illumination containing the number of modes which produces the same spatial resolution as the raster scan. This is approximately the case for $M = 17$ in Fig. 3g, for which $w_{\text{OEi},17} = 2.70 \, \mu\text{m}$ and SNR = 43.2. Compared to the 484 acquisitions for the raster scan (SNR = 17.7), the OEi image required $4 \times 17 = 68$ acquisitions, hence we achieve approximately a 7-fold compression, while the SNR is still a factor 2.5

larger.

Finally, the applicability of the method for a practical task was shown by visualising the compound distribution of a pharmaceutical sample. By increasing the number of illumination to M=16, in a ROI of $3.6 \times 3.6 \, \mu\text{m}$ a resolution of $w_{\text{OEi},16} = 0.9 \, \mu\text{m}$ can be achived allowing to visulatize even small features. We believe that OEi based indirect imaging in conjunction with Raman spectroscopy is a very promising concept for numerous real world imaging applications.

The results demonstrate high potential of the method in pharmacology, for example to detect counterfeit pharmaceuticals, monitor processes and products, and provide data for root cause analysis.

AUTHOR CONTRIBUTIONS

MM, ACDL and KD developed and planned the project. MM performed the optical eigenmode theory and algorithm design. ACDL designed the optical setup. SK simulated the illumination eigenmodes and implemented the experimental imaging algorithms. SK and SZ performed the experimental work and data analysis. All authors contributed to the discussion of the results and writing of the paper.

APPENDIX

f. Optical set-up. The experimental implementation of OEi Raman imaging is depicted in Fig. 1a: The expanded beam of a 1 W diode laser (TEC-420-0780-1000, Laser 2000, wavelength: 785 nm) is modulated by an SLM (LCOS-SLM X10468-02, Hamamatsu Photonics) and then coupled into a microscope objective ($100 \times /1.30$ Oil UPlanFL N, Olympus). The SLM is used to encode phase and amplitude onto the incident beam in first order diffraction configuration filtered by the iris [35]. The Raman scattered light from the sample is collected in epi-configuration and transmitted into a spectrograph (Shamrock SR-303i-B, Andor) equipped with a cooled

CCD detector (Newton CCD, Andor). Spectra are acquired with a 400 lines/mm grating blazed for 850 nm with a monochromator slit width of 250 µm and 5s acquisition time. The slit size was choses such that all Raman signal from the sample is collected while minimising spectral resolution loss. An LED allows white light illumination of the sample to capture transmission images on a conventional CCD camera (Basler pilot piA640-210gm, 648 × 488 pixel resolution, 7.4 µmpixel pitch).

    g. Optical eigenmodes implementation. Regarding the imaging modality, we expand the concept of optical eigenmode imaging [7] to Raman spectroscopical imaging. This technique is based on the single bucket detector measure of the optical scattering from the imaged sample under orthogonal eigenmode illumination. Conceptually, in this instance we replace the single detector by a spectrometer (see Fig. 1a) and generalise the imaging technique to scattering and conjugate focal plane detection. To illustrate these points, let us consider a set of M optical eigenmodes $\mathbb{E}_k$ (with $k = 1...M$) defining, in the sample plane, an intensity orthonormal set of optical fields

$$\int_{ROI} \mathbb{E}_j^* \mathbb{E}_k \, d\sigma = \delta_{jk} \qquad (1)$$

where ROI stands for the surface of the region of interest to be imaged. The optical eigenmodes can be determined either experimentally or theoretically. The experimental determination of the optical eigenmodes is taking into account the optical aberrations of the optical system and is equivalent to the measure of the optical transmission matrix between the spatial light modulator (SLM, see Fig. 1a) and the sample plane. However, this method is time consuming as the optical system itself needs to be experimentally characterised. If the optical set-up allows for aberration free, direct imaging and its optical transfer function is known, then it is possible to determine the set of optical eigenmodes numerically. This approach is faster though at the expense of loss of flexibility. Here, depending on the particular experiment in question, we employ both these approaches. Fig. 1b shows the precalculated OEi imaged after their propagation through the whole system and Fig. 1c verifies experimentally their orthonormality defined by equation (1).

    h. Raman imaging. The OEi imaging technique relies on the measure of the complex projection coefficients c_k corresponding to the optical overlap between the scattered field and the eigenmode illumination. These coefficients can be measured using multiple interferences between a reference beam and a OEi probe beam

$$c_k^*(\lambda) = \frac{1}{n} \sum_{p=0}^{n-1} e^{i\frac{2\pi}{n}p} \int_{ROI} s_\lambda \left| E_{\text{ref}} + e^{-i\frac{2\pi}{n}p}\mathbb{E}_k \right|^2 d\sigma$$
$$= \int_{ROI} s_\lambda E_{\text{ref}}^* \mathbb{E}_k d\sigma \qquad (2)$$

where s_λ stands for the spatially dependent incoherent Raman intensity scattering efficiency, $n \geq 3$ defines the number of phase differences used to measure the OEi projection coefficients, λ the detection wavelength defined by the spectrometer and E_{ref} the spatially dependent reference wave. In this paper, we used $n = 4$ measures for each projection coefficient accounting for the factor of four between the number illuminations and number of probes.

    Equation (2) highlights the major difference between OEi imaging in the incoherent Raman case and the coherent OEi imaging technique [7]. In the coherent case, we measure the projection coefficient in the Fourier plane of the sample, which transforms the reference beam into a single proportionality coefficient, irrespective of sample. The coefficients d_k in the coherent case are given by:

$$d_k^*(\lambda) = \frac{1}{n} \sum_{p=0}^{n-1} e^{i\frac{2\pi}{n}p} \left| \int_{\text{ROI}} T \left(E_{\text{ref}} + e^{-i\frac{2\pi}{n}p}\mathbb{E}_k \right) d\sigma \right|^2$$
$$\propto \int_{\text{ROI}} T\mathbb{E}_k d\sigma \qquad (3)$$

where T stands for the spatially dependent field transmission coefficient of the sample. Equation (3) shows that the coherent coefficients correspond to the projection coefficients of T on each of the optical eigenmodes $\mathbb{E}_k$. Therefore, the reconstructed image using these coefficients visualises the local transmission of the sample. On the other hand, we observe (Eq. (2)) that the reconstructed image using the incoherent scattering delivers the product between the local incoherent Raman scattering efficiency, s_λ, and the reference field, E_{ref}. Using a uniform illumination beam as a reference will deliver similar results in both cases. In our experiments, we therefore use a defocussed Gaussian beam as reference beam.

    As outlined above, the OEi Raman imaging process requires the determination of the complex coupling coefficient c_k with respect to a Raman band of interest for each eigenmode $\mathbb{E}_k$ illumination. Exemplarily, Fig. 2a depicts a spectrum acquired for the illumination of a polystyrene bead and a polymetacrylate (PMAA) bead with one of the eigenmodes, $\mathbb{E}_4$. The absolute value squared of the projection coefficients $|c_4|^2$ can be seen as the integral over the Raman peak of interest. In Fig. 2a the polystyrene peak is highlighted red while the PMAA peak is indicated by blue colour. Full phase and amplitude can be obtained using equation (2) with at least three differential phase steps $n = 3$. In detail, both $\mathbb{E}_k$ and E_{ref} are simultaneously encoded on the SLM using random phase encoding [36].

    After obtaining the coupling c_k for each mode $\mathbb{E}_k$, an OEi image T of the sample is formed by the superposition of the modes weighted with the corresponding coefficients:

$$T(\lambda) = \sum_{k=1}^{M} c_k(\lambda)\mathbb{E}_k \qquad (4)$$

where T corresponds in reality to $s_\lambda E_{ref}$ i.e. the reconstructed image detects the Raman scattering density illuminated by the reference beam. For comparison to the OEi images, a conventional raster scanned image can be acquired by deflecting a focused beam over the sample and capturing a Raman spectrum for each scanning position. Each pixel of the image is then formed by integration over the relevant spectral region.

[1] S. Abrahamsson, J. Chen, B. Hajj, S. Stallinga, A. Y. Katsov, J. Wisniewski, G. Mizuguchi, P. Soule, F. Mueller, C. Dugast Darzacq, X. Darzacq, C. Wu, C. I. Bargmann, D. A. Agard, M. Dahan, and M. G. Gustafsson, "Fast multicolor 3D imaging using aberration-corrected multifocus microscopy," Nat. Methods **10**, 60–63 (2012).

[2] M. G. L. Gustafsson, "Surpassing the lateral resolution limit by a factor of two using structured illumination microscopy," J. Microsc. **198**, 82–87 (2000).

[3] E. Mudry, K. Belkebir, J. Girard, J. Savatier, E. Le Moal, C. Nicoletti, M. Allain, and A. Sentenac, "Structured illumination microscopy using unknown speckle patterns," Nature Photon. **6**, 312–315 (2012).

[4] L. Shao, P. Kner, E. H. Rego, and M. Gustafsson, "Super-resolution 3D microscopy of live whole cells using structured illumination," Nature Meth. **8**, 1044–1046 (2011).

[5] S. Kosmeier, A. C. De Luca, S. Zolotovskaya, A. Di Falco, K. Dholakia and M. Mazilu, "Coherent control of plasmonic nanoantennas using optical eigenmodes," Sci. Rep. **3**, 1808 (2013).

[6] X. Tsampoula, M. Mazilu, T. Vettenburg, F. Gunn-Moore, and K. Dholakia, "Enhanced cell transfection using subwavelength focused optical eigenmode beams," Photon. Res. **1**, 42–46 (2013).

[7] A. C. De Luca, S. Kosmeier, K. Dholakia, and M. Mazilu, "Optical eigenmode imaging," Phys. Rev. A **84**, 021803 (2011).

[8] V. Ciobota, E.-M. Burkhardt, W. Schumacher, P. Rosch, K. Kusel, and J. Popp, "Applications of Raman spectroscopy to virology and microbial analysis," Anal. Bioanal. Chem. **397**, 2929–2937 (2010).

[9] P. R. Jess, M. Mazilu, K. Dholakia, A. C. Riches, and C. S. Herrington, "Optical detection and grading of lung neoplasia by Raman microspectroscopy," Int. J. Cancer **124**(2), 376–380 (2009).

[10] E. Canetta, M. Mazilu, A. C. De Luca, A. E. Carruthers, K. Dholakia, S. Neilson, H. Sargeant, T. Briscoe, C. S. Herrington, A. C. Riches, "Modulated Raman spectroscopy for enhanced identification of bladder tumor cells in urine samples," J. Biomed. Opt. **16**(3), 037002 (2011).

[11] A. C. De Luca, S. Manago, M. A. Ferrara, I. Rendina, L. Sirleto, R. Puglisi, D. Balduzzi, A. Galli, P. Ferraro, and G. Coppola, "Non-invasive sex assessment in bovine semen by Raman spectroscopy," Laser Phys. Lett. **11**(5), 055604 (2014).

[12] A. Jonas, A. C. De Luca, G. Pesce, G. Rusciano, A. Sasso, S. Caserta, S. Guido, and G. Marrucci, "Diffusive mixing of polymers investigated by Raman microspectroscopy and microrheology," Langmuir **26**(17), 14223–14230 (2010).

[13] M. Delhaye, and P. Dhamelincourt, "Raman microprobe and microscope with laser excitation," J. Raman Spectrosc. **3**(1), 33–43 (1975).

[14] S. Schlücker, M. D. Schaeberle, S. W. Huffman, and I. W. Levin, "Raman microspectroscopy: A comparison of point, line, and wide-field imaging methodologies," Anal. Chem. **75**(16), 4312–4318 (2003).

[15] S. Stewart, R. Priore, M. P. Nelson, and P. J. Treado, "Raman imaging," Annu. Rev. Anal. Chem. **5**, 337–360 (2012).

[16] N. Gierlinger, and M. Schwanninger, "The potential of Raman microscopy and Raman imaging in plant research," J. Spectrosc. **21**(2), 69–89 (2007).

[17] G. Rusciano, A. C. De Luca, G. Pesce, and A. Sasso, "Raman Tweezers as a diagnostic tool of hemoglobin-related blood disorders," Sensors **8**(12), 7818–7832 (2008).

[18] D. Graf, F. Molitor, K. Ensslin, C. Stampfer, A. Jungen, A. C. Hierold, and L. Wirtz, "Spatially resolved Raman spectroscopy of single- and few-layer graphene," Nano Lett. **7**(2), 238–242 (2007).

[19] M. N. Slipchenko, H. Chen, D. R. Ely, Y. Jung, M. T. Carvajal, and J.-X. Cheng, "Vibrational imaging of tablets by epi-detected stimulated Raman scattering microscopy," Analyst **135**(10), 2613–2619 (2013).

[20] K. Hamada, K. Fujita, N. I. Smith, M. Kobayashi, Y. Inouye, and S. Kawata, "Raman microscopy for dynamic molecular imaging of living cells," J. Biomed. Opt. **13**(4), 044027 (2008).

[21] A. F. Palonpon, J. Ando, H. Yamakoshi, K. Dodo, M. Sodeoka, S. Kawata, and K. Fujita, "Raman and SERS microscopy for molecular imaging of live cells," Nat. Protoc. **8**(4), 677–692 (2013).

[22] P. J. Treado, and M. D. Morris, "Hadamard transform Raman imaging," Appl. Spectrosc. **42**(5), 897–901 (1988).

[23] G. J. Puppels, M. Grond, and J. Greve, "Direct imaging Raman microscope based on tunable wavelength excitation and narrow-band emission detection," Appl. Spectrosc. **47**(8), 1256–1267 (1993).

[24] P. J. Treado, I. W. Levin, and E. N. Lewis, "High-fidelity Raman imaging: a rapid method using an acousto-optic tunable filter," Appl. Spectrosc. **46**(8), 1211–1216 (1992).

[25] R. W. Havener, S.-Y. Ju, L. Brown, Z. Wang, M. Wojcik, C. S. Ruiz-Vargas, and J. Park, " High-throughput graphene imaging on arbitrary substrates with widefield Raman spectroscopy," ACS Nano **6**(1), 373–380 (2012).

[26] B. M. Davis, A. J. Hemphill, D. C. Maltaş, M. A. Zipper, P. Wang, and D. Ben-Amotz, "Multivariate hyperspectral Raman imaging using compressive detection," Anal. Chem. **83**(13), 5086–5092 (2011).

[27] V. Studer, J. Bobin, M. Chahida, H.S. Mousavia, E. Candes, and M. Dahane, "Compressive fluorescence microscopy for biological and hyperspectral imaging," Proc. Natl. Acad. Sci. USA **109**, E1679–E1687 (2011).

[28] J. H. Shapiro, "Computational ghost imaging," Phys. Rev. A **78**, 061802 (2008).

[29] Y. Bromberg, O. Katz, and Y. Silberberg, "Ghost imaging with a single detector," Phys. Rev. A **79**, 053840

(2009).

[30] M. Mazilu, J. Baumgartl, S. Kosmeier, and K. Dholakia, "Optical eigenmodes; exploiting the quadratic nature of the energy flux and of scattering interactions," Opt. Express **19**, 933–945 (2011).

[31] W. D. Montgomery, "Phase retrieval and the polarization identity," Opt. Lett. **2**, 120–121 (1978).

[32] N. Guarrotxena, Y. Ren, and A. Mikhailovsky, "Raman response of dithiolated nanoparticle linkers," Langmuir **27**, 347–351 (2010).

[33] L. Li, T. Hutter, A. S. Finnemore, F. M. Huang, J. J. Baumberg, S. R. Elliott, U. Steiner, and S. Mahajan, "Metal oxide nanoparticle mediated enhanced Raman scattering and its use in direct monitoring of interfacial

chemical reactions," Nano Lett. **12**, 4242–4246 (2012).

[34] P. Ferraro, S. De Nicola, A. Finizio, G. Coppola, S. Grilli, C. Magro, and G. Pierattini, "Compensation of the inherent wave front curvature in digital holographic coherent microscopy for quantitative phase-contrast imaging," Appl. Opt. **42**(11), 1938–1946 (2003).

[35] J. Davis, D. Cottrell, J. Campos, M. Yzuel, and I. Moreno, "Encoding amplitude information onto phase-only filters," Appl. Opt. **38**(23), 5004–5013 (1999).

[36] B. Katz, J. Rosen, R. Kelner, and G. Brooker, "Enhanced resolution and throughput of Fresnel incoherent correlation holography (FINCH) using dual diffractive lenses on a spatial light modulator (SLM)," Opt. Express **20**, 9109–9121 (2012).